coatings

MDPI

Article

Effect of Polarity on Arc Ablation Behaviour and Damage Mechanisms of Brush/Slip Ring Contact Interfaces

Wanting Li [1], Xinze Zhao [1,*], Wei Yang [2], Xiang Xu [1] and Xiaolong Zhang [1]

[1] College of Mechanical and Power Engineering, China Three Gorges University, Yichang 443002, China; 202408020021507@ctgu.edu.cn (W.L.)
[2] Innovation and Entrepreneurship College, China Three Gorges University, Yichang 443002, China
* Correspondence: xzzhao@ctgu.edu.cn; Tel.: +86-13972603535

Abstract

To clarify the origin of asymmetric arc ablation in hydroelectric generator slip rings, a Steel 45/carbon current-carrying friction pair was selected to investigate the influence of current polarity on arc behaviour and interfacial damage. Static gap discharge tests (10 A) and dynamic tests (current density of 10 A/cm^2, sliding velocity of 0.419 m/s) were performed to characterize polarity-dependent erosion behaviour. The results indicate that, under the steel(+)–carbon(−) condition, the arc exhibits unstable burst-like discharge accompanied by intense spark spattering. The carbon cathode experiences severe material loss due to the combined effects of cathode-spot heating, positive-ion bombardment, and molten metal droplet impact. The steel surface is characterized by nested erosion pits and spherical resolidified spatter particles, while the apparent ablation-affected area shows an overall increase with accumulated arc duration, with a more pronounced expansion observed at longer durations. Pronounced bidirectional material migration and interfacial elemental enrichment are observed under the steel(+)–carbon(−) configuration, resulting in an apparent net mass loss rate approximately 2.5 times higher than that under the steel(-)–carbon(+) configuration. The reversed steel(−)–carbon(+) configuration produces a spatially constrained and stable arc discharge, accompanied by a continuous remelted layer and network-like thermal-stress cracks on the steel surface. Polarity reversal changes the direction of the interfacial electric field and charged-particle migration, thereby regulating cathode electron emission, arc discharge behaviour, energy distribution in the near-electrode region, and bidirectional material migration across the interface. These results provide a theoretical basis for elucidating the polarity-dependent arc ablation mechanism of steel/carbon friction pairs and for optimizing polarity configuration and differentiated protection strategies for hydroelectric generator slip rings.

Keywords: arc discharge; polarity effect; current-carrying friction; steel/carbon friction pair; interface erosion damage

Check for updates

Academic Editor: Charafeddine Jama

Received: 29 June 2026
Revised: 5 August 2026
Accepted: 6 August 2026
Published: 10 August 2026

Copyright: © 2026 by the authors. Licensee MDPI, Basel, Switzerland. This article is an open access article distributed under the terms and conditions of the Creative Commons Attribution (CC BY) license.

1. Introduction

In the excitation system of a hydroelectric generator, the positive and negative slip rings are arranged in symmetrical pairs with carbon brushes and operate synchronously under identical operating parameters and environmental conditions [1]. However, during actual operation, arcing frequently occurs at the contact surfaces between the carbon brushes and the slip rings [2–4], with the surface of the positive slip ring often exhibiting more severe ablation characteristics [5]. This asymmetric damage phenomenon cannot be

explained solely by differences in mechanical or electrical operating conditions, suggesting that polarity-induced variations in arc behaviour and interfacial material response may play an important role. However, the underlying mechanism governing polarity-dependent arc ablation remains unclear.

Current-carrying friction pairs typically operate in rolling or sliding contact modes. The introduction of electric current significantly increases the complexity of friction and wear behaviour at the contact interface [6]. Under current-carrying conditions, wear mechanisms can be mainly classified into four categories: mechanical wear, electrical wear, chemical wear, and multi-mechanism coupled wear [7,8]. Among them, electrical wear is predominantly driven by arc ablation, which manifests as material spattering, melting, vapourization and other damage forms, with its action characteristics determined by the intrinsic properties of the materials. Meanwhile, arc ablation further amplifies the effects of other wear mechanisms and exacerbates the overall damage to the contact interface [9]. Under severe operating conditions, contact instability becomes one of the main causes of arcing in current-carrying friction; arcing caused by gap breakdown results in thermal damage to the electrode surface, exacerbating wear and degrading system performance [10–13]. Previous studies have investigated arc discharge from various perspectives. Deng et al. [14] revealed that arc discharge undergoes two evolution stages: initially, the arc is constrained above the friction surface due to the narrow gap, resulting in a relatively small discharge region; subsequently, the arc moves toward the exit of the pin specimen, where it becomes less constrained and develops into a fan-shaped structure before extinction. They further found that arc ablation is more severe at the exit region than at the entrance. Yang et al. [15] demonstrated that arc discharge migrates along the sliding direction, and the associated thermal accumulation and sputtering effects induce material melting, evapouration, and oxidation, thereby accelerating surface degradation. In addition to arc evolution behaviour, researchers have also investigated the relationship between arc discharge and wear degradation. Zhang et al. [16] found that arc occurrence exhibits periodic synchronization with contact force, and increasing arc initiation frequency promotes the transition of the dominant wear mechanism from mechanical wear to arc ablation. Tang et al. [17] further studied the influence of slip ring materials on arc erosion resistance and proposed three stages of arc damage evolution, namely constriction heating, incandescent melting, and arc erosion. They reported that CuW70 exhibited superior arc erosion resistance due to the restriction effect of its tungsten skeleton on molten pool expansion, whereas 7075Al suffered more severe damage because of its low-melting-point matrix. Besides material properties, electrode polarity is another important factor affecting arc-induced damage. Jin [18], Liu [19] and co-workers investigated polarity-dependent arc ablation in carbon–copper electrical contacts and found that electrode polarity significantly influenced the ablation behaviour of both electrodes under opposite polarity conditions. They also observed material transfer from the anode to the cathode under both polarity conditions. Nevertheless, these studies mainly focused on carbon–copper electrical contacts, and the polarity-dependent asymmetric damage mechanism of steel–carbon friction pairs remains insufficiently understood.

Despite previous studies on polarity-dependent arc damage [20,21] the mechanism by which electrode polarity affects arc behaviour and leads to asymmetric damage in steel–carbon friction pairs remains insufficiently understood. In this study, a Steel 45 (GB/T 699-2015)/carbon friction pair was selected as the test specimen, and a non-contact pure-gap arc ablation test was designed to eliminate the influence of mechanical friction and investigate the intrinsic effect of electrode polarity on arc erosion. By systematically analysing arc characteristics, surface morphology, and material damage under different polarity conditions, this study aims to elucidate the polarity-dependent asymmetric arc

ablation behaviour and its underlying mechanisms, providing deeper insights into arc-induced degradation in current-carrying friction systems.

2. Experimental

2.1. Materials and Preparation

A disc-pin friction pair was used in this study, with the disc specimen made of Steel 45 (⌀ 40 mm × 2 mm), and the pin specimen was a Shanghai Morgan D172 carbon brush (5 mm × 5 mm × 20 mm). This metal/carbon friction pair is representative of the electrical contact materials used in hydroelectric generator slip-ring systems. The steel disc was progressively ground and polished using 600–2000 grit sandpaper, followed by ultrasonic cleaning in ethanol for 10 min to remove surface impurities. Finally, the three-dimensional morphology of the original specimen was measured using a 3D profilometer, and the scanning electron microscope (SEM) morphology is shown in Figure 1.

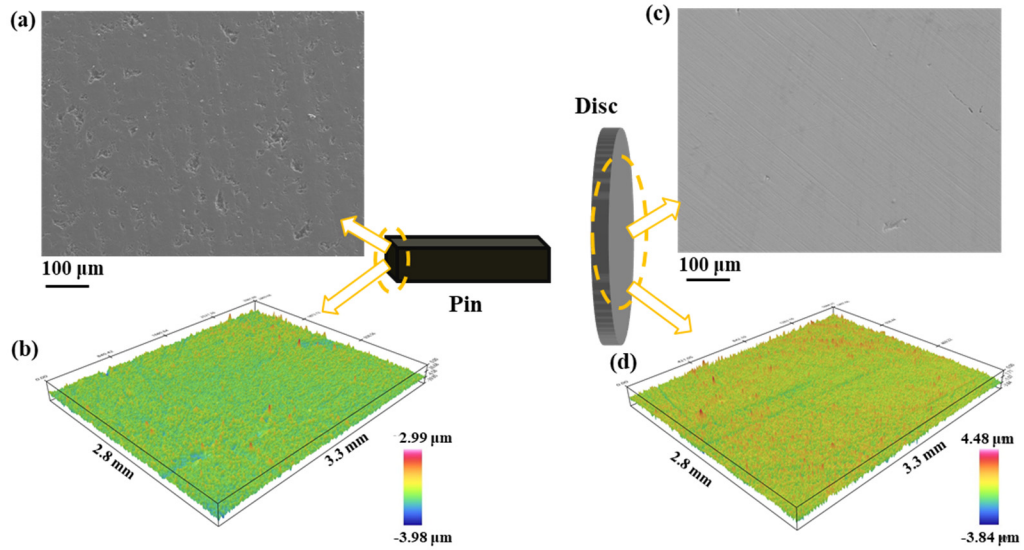


Figure 1. Original surface morphology of friction pair specimens: (**a**) SEM image of carbon pin; (**b**) 3D morphology of carbon pin; (**c**) SEM image of steel disc; (**d**) 3D morphology of steel disc.

2.2. Experimental Methods

Two complementary non-contact experimental configurations were employed. The static gap-discharge test was designed to investigate the fundamental influence of electrode polarity on arc evolution and early-stage surface damage under a stationary condition. The rotating gap-discharge test was conducted with the steel disc rotating beneath the carbon brush while a constant interelectrode gap was maintained. This configuration introduced circumferential relative motion without direct mechanical contact, enabling the cumulative arc-induced damage under rotating conditions to be evaluated independently of mechanical friction and contact wear. In both configurations, the steel disc and carbon brush remained physically separated throughout the test; therefore, no normal load was applied and mechanical sliding wear was excluded.

The tests were conducted on a custom-built current-carrying friction and wear testing machine, as shown in Figure 2. During the tests, the gap distance between the electrodes was controlled precisely. Two polarity configurations were tested: steel(+)–carbon(−) and steel(−)–carbon(+). The polarity was controlled by connecting the steel disc to the positive or negative terminal of the DC power supply, while the carbon brush was connected oppositely. Each operating condition was repeated three times.

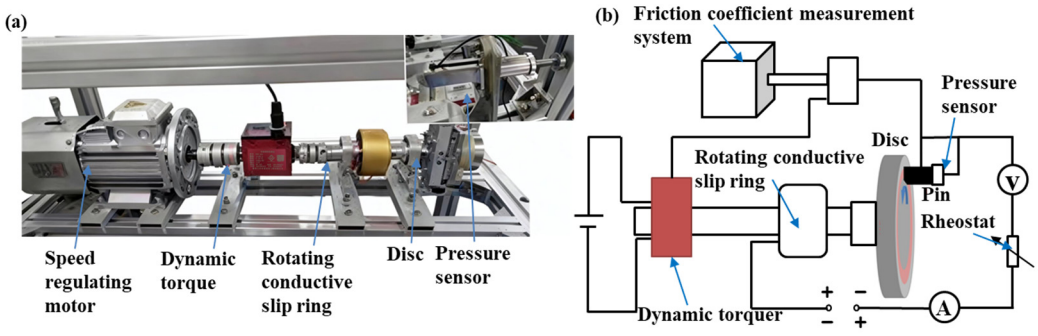


Figure 2. Experimental setup: (**a**) current-carrying friction and wear tester; (**b**) schematic diagram of test system.

Specific procedure for the static gap test: A Steel 45 disc and a carbon brush were clamped onto the testing machine. After a current of 10 A was applied, the gap between the brush and the ring was slowly increased with a precision displacement stage; movement was halted when the gap reached 0.2 mm and stable arc discharge was generated, as shown in Figure 3. This gap distance was selected based on preliminary tests, which demonstrated that a 0.2 mm gap enabled stable arc ignition and sustained discharge under the applied current while avoiding direct mechanical contact between the two electrodes. Therefore, the influence of mechanical wear could be minimized, allowing the intrinsic effect of electrode polarity on arc-induced damage to be evaluated. The arc morphology was recorded throughout the process with a Thousand-Eye Wolf high-speed camera (frame rate 1000 fps). To investigate the effect of accumulated arc duration on damage to the steel surface, the accumulated arc duration was set to 1, 3, 5, 7 and 10 s respectively; the test parameters are shown in Table 1. Following the test, the ablated surface was examined for morphology and analysed for composition.

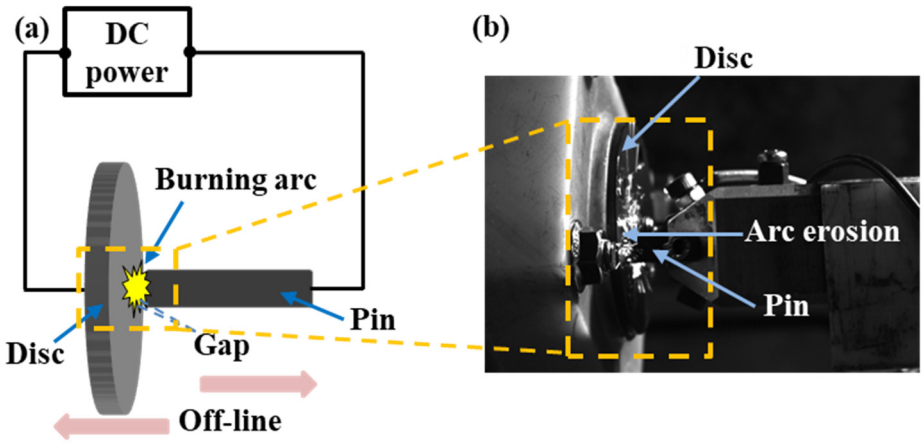


Figure 3. Gap arc breakdown of the friction pair: (**a**) schematic diagram; (**b**) physical photograph.

Table 1. Experimental parameters.

Test	Parameters				
	Polarity	Current/A	Current Density/A × cm^{-2}	Rotational Speed/rpm	Accumulated Arc Duration/s
Static gap test	+, −	10	—	—	1, 3, 5, 7, 10
Dynamic test	+, −	2.5	10	200	300

Specific steps for the dynamic test: the steel disc and carbon brush were separated by a fixed interelectrode gap of 0.2 mm, which was set using the precision displacement stage

and maintained throughout the test. The steel disc was operated at 200 rpm, corresponding to a peripheral velocity of 0.419 $m \cdot s^{-1}$ at the test track, and a current of 2.5 A was applied. Based on the 5 mm × 5 mm cross-sectional area of the carbon brush, the corresponding nominal current density was 10 $A \cdot cm^{-2}$. No normal load was applied because the two electrodes remained physically separated during the entire test. Under rotation, the relative position between the steel surface and the carbon brush continuously changed, and the arc exhibited intermittent extinction and reignition despite the constant geometric gap. When the accumulated arc-on duration reached 300 s, the power supply was switched off and the rotation was stopped. The accumulated arc duration was defined as the cumulative sum of the individual arc-on periods recorded during the entire test. After testing, the ablated surfaces of the steel disc and carbon brush were examined for morphology and elemental composition.

2.3. Characterisation Methods

The dynamic behaviour of the arc was recorded using a Thousand-Eye Wolf high-speed camera (1000 fps). The macroscopic features of the ablated regions were examined by optical imaging, while the microscopic morphologies were characterized using scanning electron microscopy (SEM, Zeiss Sigma 300). The ablated area was quantitatively measured using a 3D profilometer (Sensofar S Neox). Elemental distribution and material transfer behaviour were analysed using energy-dispersive X-ray spectroscopy (EDS, Xplore 30).

The mass difference of carbon brushes before and after arc discharge was measured using an electronic balance (FB-224, precision: 0.1 mg), and the net mass change rate W_m ($g \cdot (A \times h)^{-1}$) was calculated as $W_m = \Delta m/(I \times t)$, where Δm is the mass difference in the specimen before and after the test (g), I is the direct current in the test circuit (A), and t is the accumulated arc duration (h).

3. Results and Discussion

3.1. Arc Behaviour and Surface Ablation in Static Tests

Through static gap tests, this study investigated the mechanisms governing the full-cycle dynamic behaviour of arc initiation, development and extinction during the breakdown process of steel/carbon friction pairs, analysed the macroscopic ablation morphology on the surfaces of positive and negative steel electrodes under different arc durations, and established the intrinsic relationship between arc dynamics and macroscopic damage at the interface.

3.1.1. Dynamic Arc Evolution Characteristics

Figures 4 and 5 show the complete evolution of a single-pulse arc when the steel disc is connected to the positive and negative terminals, respectively.

For steel(−)–carbon(+), the duration from arc initiation to extinction was 9 ms. At t = 0.030 s, the arc broke through the separation gap of the friction pair and ignited, first forming a short, thick, and regularly shaped columnar arc at the top of the steel/carbon gap. The arc column was strongly spatially confined and showed no significant diffusion; following ignition, the columnar arc rapidly contracted into a slender filamentary form, white fume appeared above the arc column, which may have resulted from the combined effects of rapid condensation of surrounding moisture and the formation of fine particles from evapourated electrode materials under the high-temperature arc environment; as the contact gap slowly increased, the arc morphology transformed from filamentary to fan-shaped, with the brightness of the arc column increasing simultaneously; subsequently, the spatial coverage of the fan-shaped arc expanded until, at t = 0.037 s, the arc first broke

and extinguished at the corners of the fan, with brightness rapidly decaying and the discharge ending.

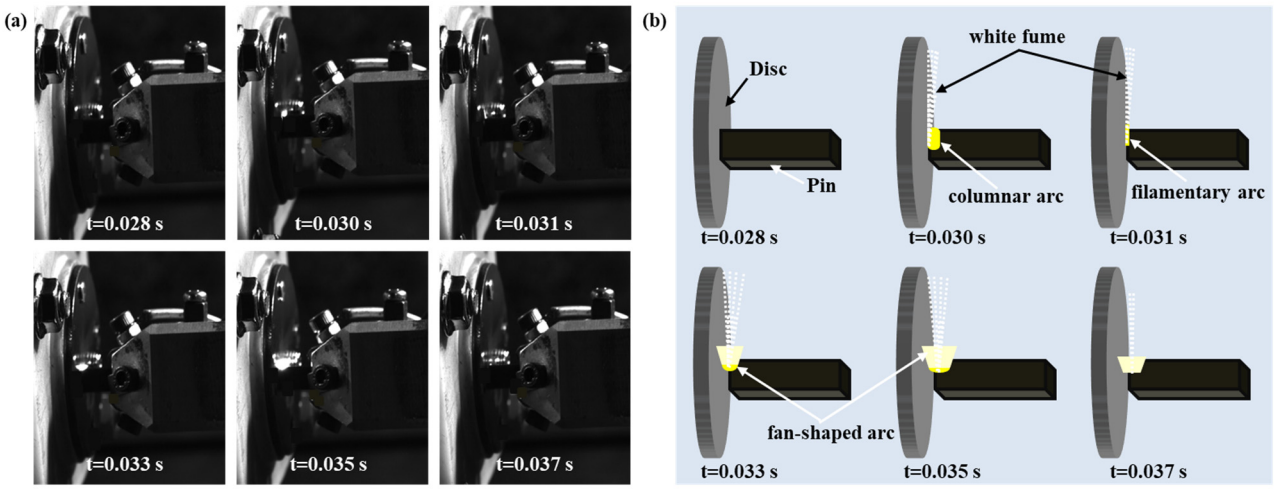


Figure 4. Dynamic evolution of single-pulse arc discharge under steel(-)–carbon(+) configuration: (**a**) physical photograph; (**b**) schematic diagram.

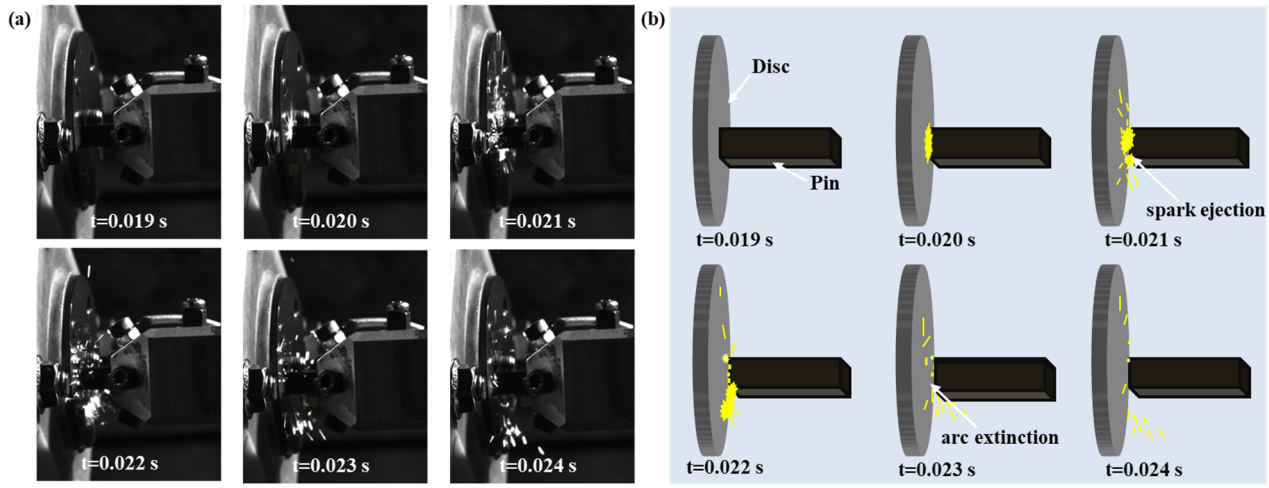


Figure 5. Dynamic evolution of single-pulse arc discharge under steel(+)–carbon(−) configuration: (**a**) physical photograph; (**b**) schematic diagram.

For steel(+)–carbon(−), the duration from arc initiation to extinction was 5 ms, of which the effective arc burning time was only 3 ms, with the remaining time comprising the decay and extinction process of spattered sparks. At t = 0.020 s, gap breakdown occurred at the steel/carbon contact surface, instantly generating a strong arc discharge. The initial arc column exhibited an irregular radial pattern, with the luminous coverage extending up to twice the area of the contact surface, and the brightness rose rapidly; immediately after the arc was established, explosive sputtering of sparks occurred, accompanied by the ejection of molten material, further increasing the brightness of the arc column; at t = 0.022 s, the arc column detached from the lower region of the contact surface while remaining in a burning state without extinguishing; by the next millisecond, the arc column had completely disappeared, and for the remainder of the time, only the gradual fading of the already-spattered molten sparks until complete extinction could be observed.

These different arc evolution characteristics indicate that electrode polarity affects the spatial distribution and stability of arc energy input. The relatively confined arc under steel(−)–carbon(+) provides a stable thermal loading condition, whereas the ex-

plosive arc under steel(+)–carbon(−) produces stronger localised energy concentration and material ejection.

3.1.2. Temporal Evolution of Steel Surface Erosion

Figure 6 shows a comparison of the arc ablation morphologies on the surfaces of steel discs under two polarities, observed using an optical microscope (×50) for different arc durations (1 s, 3 s, 5 s, 7 s, 10 s). There were significant differences in the ablation morphologies between the two polarities:

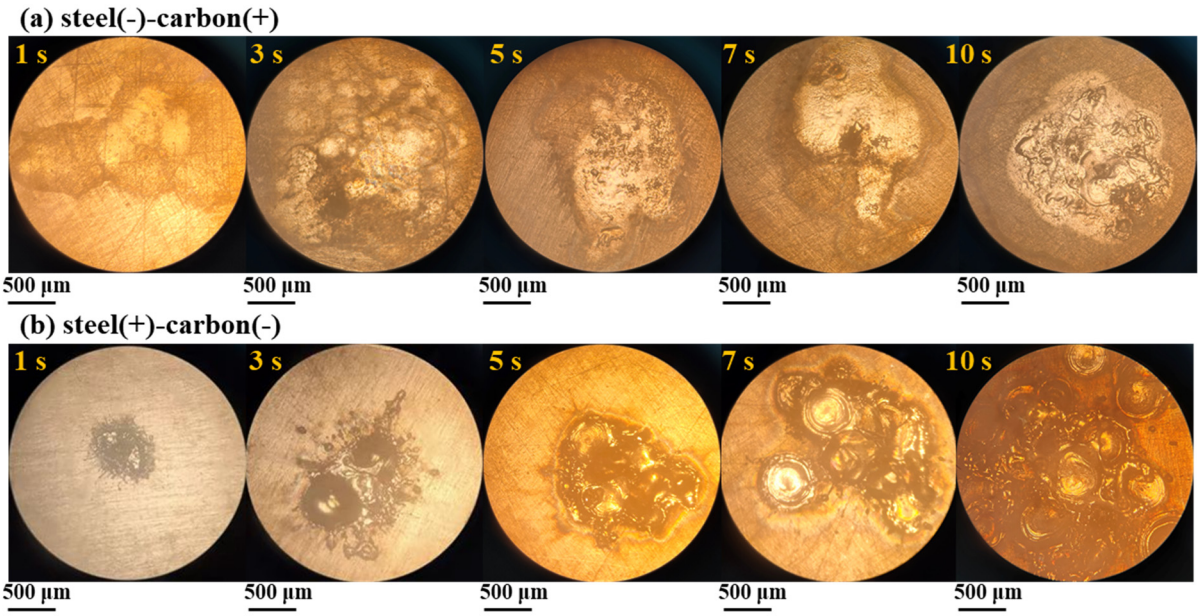


Figure 6. Macroscopic morphology of arc-ablated regions on steel surfaces at different arc durations: (**a**) steel(−)–carbon(+); (**b**) steel(+)–carbon(−).

For steel(−)–carbon(+), only localised thermal oxidation and slight surface modification occurred at 1 s; as the arc duration increased, shallow melt spots and a distinct heat-affected zone formed;

For steel(+)–carbon(−), an ablation core and radial spatter marks formed within 1 s and the ablation area expanded rapidly over time. After 10 s of arc burning, the steel surface was covered by a molten and resolidified layer containing nested molten pits, and the extent of damage was far greater than that observed for steel(−)–carbon(+) under the same duration. These macroscopic morphological differences were highly consistent with the dynamic arc behaviour shown in Figures 4 and 5.

Three-dimensional topographical scans were performed on the ablation zones of the steel discs under different arc durations and polarity configurations, and the corresponding apparent ablation areas were quantified, as presented in Figure 7.

For the steel(−)–carbon(+) configuration, the apparent ablation area expanded rapidly from 1 to 3 s, temporarily decreased during the period from 3 to 7 s, and then increased sharply from 7 to 10 s. This temporary decrease may not necessarily indicate a reduction in damage severity because the identified boundary of the topographically altered region may be influenced by remelted and resolidified materials and transferred products that partially obscure shallow ablation features. Therefore, surface remelting, resolidification, and material deposition are considered possible contributors to the observed fluctuation. With extended arc duration, accumulated thermal damage and surface cracking may have increased the spatial extent of the identifiable affected region, corresponding to the renewed increase in the apparent ablation area.

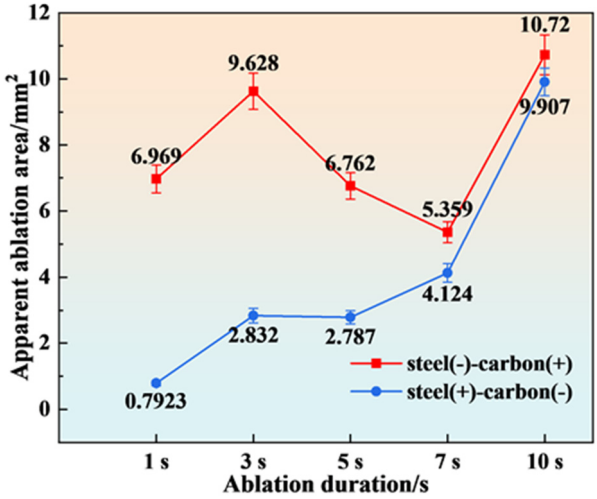


Figure 7. Variation in the apparent ablation area with accumulated arc duration.

For the steel(+)–carbon(−) configuration, the apparent ablation area showed an overall increasing tendency with accumulated arc duration. The measured areas at 3 and 5 s were comparable, at 2.832 and 2.787 mm^2, respectively, indicating an approximately stable interval within the experimental scatter rather than a strictly monotonic increase. A more pronounced expansion was subsequently observed from 7 to 10 s. The relatively limited variation during the earlier stage may be associated with the gradual development of molten and oxidized regions, whereas the more pronounced expansion at longer durations is consistent with repeated melting, spattering, and material removal under prolonged arc exposure.

3.2. Arc Ablation Characteristics in Dynamic Tests

The dynamic test was conducted under a fixed-gap, non-contact condition. Therefore, the observed circumferential damage should be interpreted as arc-induced ablation associated with disc rotation rather than mechanical sliding wear. Rotation continuously changed the position of the steel surface relative to the carbon brush and consequently altered the spatial distribution of arc attachment and heat input. The polarity-dependent carbon-brush net mass change and surface morphology obtained under this controlled rotating condition are analysed below.

3.2.1. Carbon Brush Net Mass Change

To evaluate the polarity-dependent variation in carbon brush mass change, three parallel tests were conducted for each polarity condition. The results are shown in Tables 2 and 3. Considering the porous structure of graphite, the measured mass change may include not only arc-induced material loss but also the evapouration of adsorbed moisture during arc exposure. Therefore, the obtained values represent the net mass change in the carbon brush electrodes. Under identical test conditions:

Table 2. Mass change of carbon brushes under steel(-)–carbon(+) configuration.

Parameter	Steel(−)–Carbon(+) 1	Steel(−)–Carbon(+) 2	Steel(−)–Carbon(+) 3
Mass before test/g	1.009	0.9763	1.0872
Mass after test/g	1.0083	0.9754	1.0863
Mass change/g	0.0007	0.0009	0.0009
Net mass change rate/g/(A × h)	0.00336	0.00432	0.00432

Table 3. Mass change of carbon brushes under steel(+)–carbon(-) configuration.

Parameter	Steel(+)–Carbon(−) 1	Steel(+)–Carbon(−) 2	Steel(+)–Carbon(−) 3
Mass before test/g	1.0285	1.1182	1.0476
Mass after test/g	1.0266	1.1161	1.0465
Mass change/g	0.0019	0.0021	0.0021
Net mass change rate/g/(A × h)	0.00912	0.01008	0.01008

For steel(−)–carbon(+), the average mass change in the carbon brush was 0.00083 g, with an average net mass change rate of only 3.9×10^{-3} g/(A × h). This slight decrease may be partially attributed to moisture evapouration from the porous graphite structure rather than solely to arc-induced material removal.

For steel(+)–carbon(−), the average mass change in the carbon brush reached 0.0020 g, with an average net mass change rate of 9.76×10^{-3} g/(A × h), approximately 2.5 times higher than that under the carbon-anode condition.

When the carbon brush acts as the cathode in the steel (+)–carbon (−) configuration, high-energy positive ions accelerate across the cathode sheath and bombard the carbon surface, inducing localised heating and sputtering. The low thermal conductivity and porous structure of graphite may influence cathode spot behaviour and contribute to localised energy accumulation. Consequently, carbon degradation may be promoted through sublimation and oxidation-related processes. Meanwhile, iron-containing species generated from the steel electrode can migrate toward and deposit on the carbon surface, partially compensating for carbon loss. These combined effects result in a higher measured net mass loss rate of the carbon brush.

3.2.2. Steel Surface Macroscopic Morphology Differences

Figure 8 shows the overall morphology of the steel disc after ablation, as well as the macroscopic morphology of the corresponding region under a 50× magnification electron microscope.

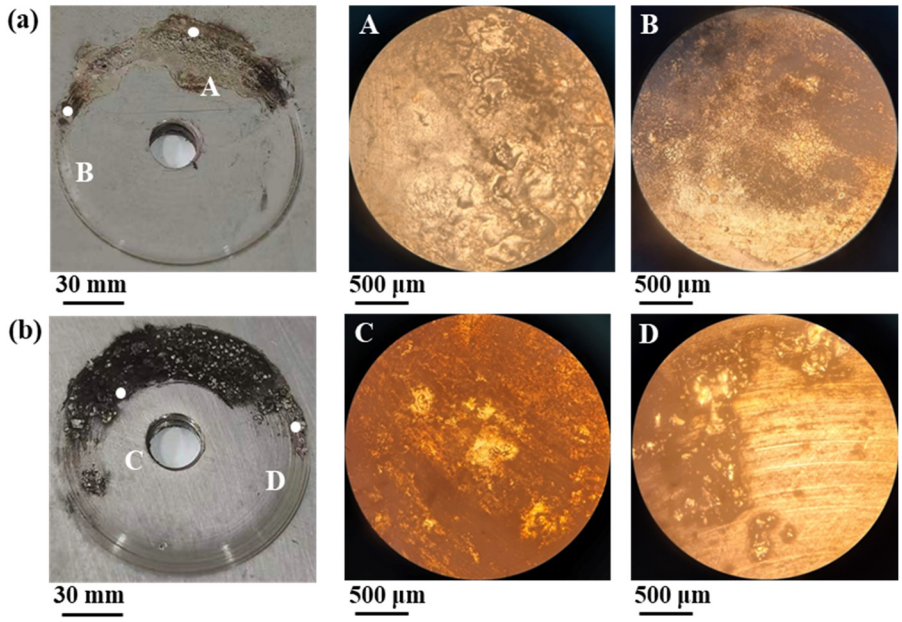


Figure 8. Macroscopic morphology of the arc ablation zone on the steel surface following dynamic arc ablation: (**a**) steel(-)–carbon(+), A, core ablation zone; B, peripheral ablation zone; (**b**) steel(+)–carbon(-), C, core ablation zone; D, peripheral ablation zone.

For the steel(−)–carbon(+), the arc ablation zone was concentrated and distributed in an arc-shaped band extending along the circumference, with the band length accounting for approximately one-third of the total circumference. The overall morphology was relatively continuous and smooth; the main ablation zone appeared light brown (a colour resulting from thermal oxidation), with a clear but irregular boundary with the unablated matrix region. Dark brown to black regions at the ends of the ablation band were observed, which were mainly attributed to deposited carbonaceous products based on the subsequent elemental analysis. At point A in the core region, the steel surface was covered by a molten layer, exhibiting a wrinkled texture formed by the flow and cooling of molten metal, accompanied by irregular bubble-like pits. At point B in the transition zone, the surface undulations were gentler, with no obvious molten layer or pits, and black patchy areas were observed.

For the steel(+)–carbon(−), the arc ablation zone was distributed as a continuous, wide band along the upper semicircle of the steel disc, with the band length accounting for approximately half of the total circumference; the boundary with the unablated matrix region was clear and regular. The ablated area was mainly dark black and covered with abundant powdery deposits. The surface roughness and degree of morphological modification were higher than those observed under the steel(−)–carbon(+) condition. At point C in the core region, the molten region was accompanied by abundant black powdery deposits and solidified products. At point D in the peripheral region, discontinuous molten traces with fragmented boundaries were observed, together with slight thermal oxidation discoloration and a small amount of carbon-containing deposits.

3.3. Microstructure and Elemental Distribution

3.3.1. Static Test Results

Figure 9 shows SEM morphologies (×50, ×200) of ablated regions on steel surfaces with different polarities. For steel(−)–carbon(+), after 1 s arc duration, localised shallow melt spots were observed at low magnification. The matrix integrity remained relatively intact, with only slight heat-affected regions surrounding the melt spots. A small number of shallow pits were distributed sporadically within the affected region. At high magnification, fine cracks, shallow pits, and a few white granular particles were observed near the melt spots.

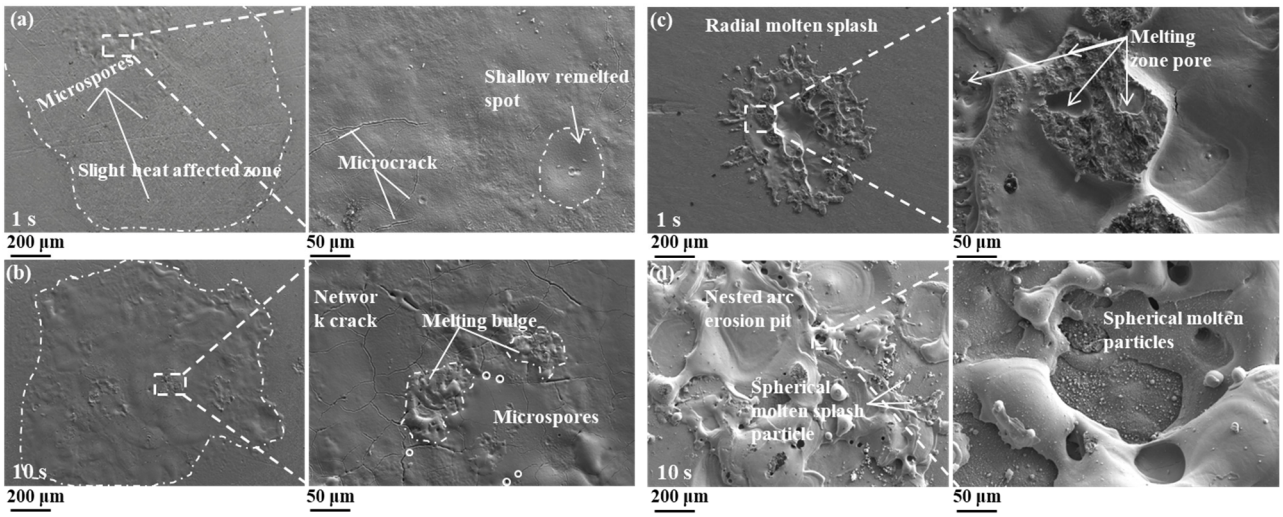


Figure 9. Microscopic morphology of steel surfaces after static tests: (**a**) 1 s, steel as cathode; (**b**) 10 s, steel as cathode; (**c**) 1 s, steel as anode; (**d**) 10 s, steel as anode.

After 10 s arc duration, a continuous remelted layer was formed on the steel surface. Under high magnification, the surface of the remelted layer exhibited molten protrusions generated during melt flow and subsequent solidification, together with several micropores and thermal cracks. These features indicate repeated thermal effects and solidification processes during arc exposure.

For steel(+)–carbon(−): just 1 s arc duration, localised melt pits appeared on the steel surface, with a clear boundary between the ablated core and the unablated matrix. Compared with steel(−)–carbon(+), the damage was more concentrated and the surface modification was more pronounced. Under high magnification, a distinct molten depression formed in the ablated core area, with molten voids visible within the pit.

After 10 s arc duration, the steel surface exhibited an expanded damaged region containing multiple overlapping arc-induced pits. The pits were large in size, with spherical molten spatter particles distributed around their edges. The original surface morphology was significantly modified. Under high magnification, spherical particles, molten flow traces, pores, and irregular protrusions were observed within and around the erosion pits, indicating repeated melting, material ejection, and resolidification during arc exposure.

Surface elemental scanning EDS analysis was performed on the ablated core regions of steel surfaces subjected to 10 s arc discharge under different polarities, as shown in Figure 10. The elemental composition of the original unablated Steel 45 surface was 92 wt.% Fe, 6.5 wt.% C and 1.5 wt.% O. For steel(−)–carbon(+), C was locally enriched in the molten zone, with its content rising to 17 wt.%, whilst the O content remained nearly unchanged compared to the unablated matrix. For steel(+)–carbon(−), C and O were enriched in the molten pit and spheroidal particle zones, with concentrations of 25.3 wt.% and 5.1 wt.% respectively. The increased C concentration indicates the deposition of carbon-containing species on the steel anode surface, whereas the elevated O content may be associated with oxidation reactions involving the high-temperature steel surface and deposited carbon species under atmospheric conditions.

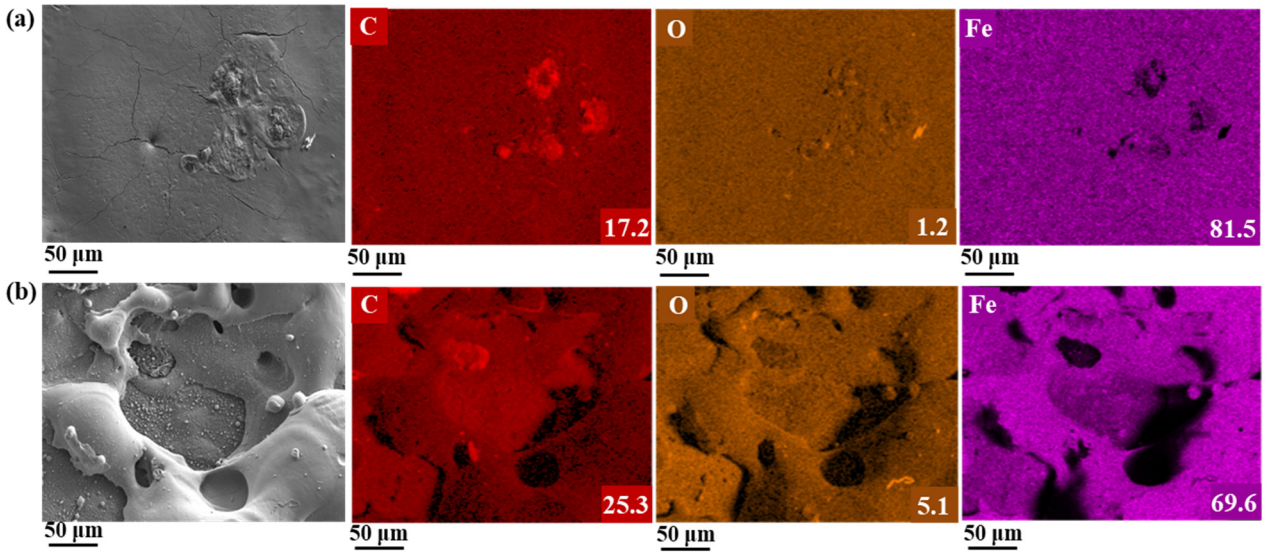


Figure 10. Elemental distribution and concentrations in the core ablation zone of steel surfaces after 10 s arcing: (**a**) steel as cathode; (**b**) steel as anode.

Figure 11 illustrates the effect of polarity on the surface morphology of the carbon brush, and Figure 12 provides an analysis of the elemental distribution on the brush surface based on energy dispersive spectroscopy (EDS) data. The elemental composition of the original carbon brush matrix is 98.5 wt.% C, 1.2 wt.% O and 0.3 wt.% Fe. For steel(−)–carbon(+), only limited micropore expansion and graphite-layer spalling were observed

after short-term arc exposure. After 10 s, the affected regions expanded, although the overall morphological alteration remained relatively limited. The selected-area EDS result showed 96.7 wt.% C and 2.4 wt.% Fe, indicating only limited local enrichment of Fe-containing material on the carbon surface.

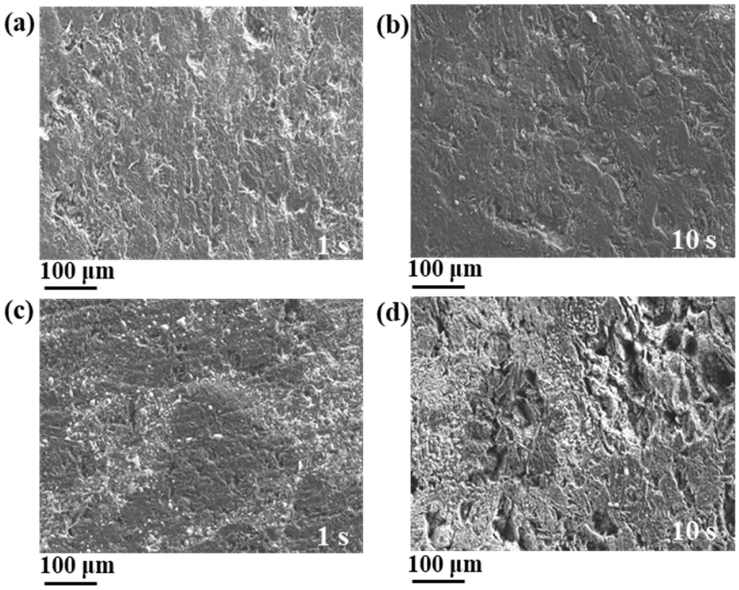


Figure 11. Microscopic morphology of carbon brush surfaces after static tests: (**a**) 1 s, carbon as anode; (**b**) 10 s, carbon as anode; (**c**) 1 s, carbon as cathode; (**d**) 10 s, carbon as cathode.

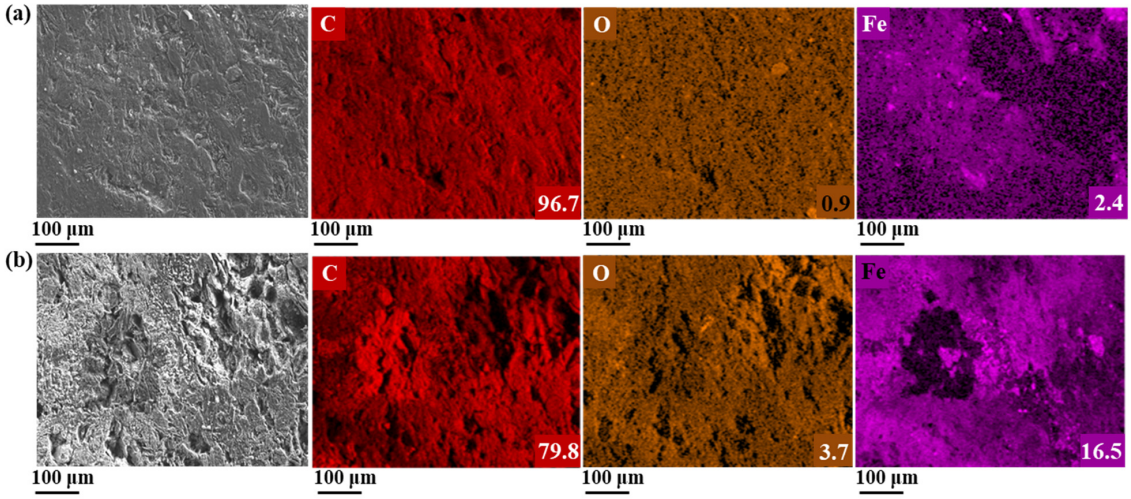


Figure 12. Elemental distribution and concentrations in the core ablation zone of carbon brush surfaces after 10 s arcing: (**a**) carbon as anode; (**b**) carbon as cathode.

For steel(+)–carbon(−), a large number of spherical or irregularly shaped white particles adhered to the carbon surface after just 1 s of arc burning; after 10 s of arc burning, the carbon brush matrix was severely damaged, with multiple irregular erosion pits forming on the surface and localised non-uniform material removal occurring. EDS analysis showed that the Fe content rose from the initial 0.3 wt.% to 16.5 wt.%, the C content fell to 79.8 wt.%, and the O content rose slightly to 3.7 wt.%. The significant increase in Fe content on the carbon surface indicates that metallic species generated from steel ablation migrated toward and deposited on the carbon electrode.

The complementary elemental-enrichment patterns observed on the two electrode surfaces provide evidence consistent with bidirectional interfacial material transfer during

arc discharge. The enrichment of C on the steel surface is consistent with the transfer of carbon-containing species from the carbon electrode, whereas the enrichment of Fe on the carbon surface supports the transfer of Fe-containing species from the steel electrode. The specific physical forms of the transferred species, such as vapour, fine particles, or molten droplets. Their transport may be influenced by plasma flow, electromagnetic forces, and the high-temperature state of the electrode surfaces.

3.3.2. Dynamic Test Results

Figure 13 shows SEM morphologies (×50, ×200) of the ablated regions on steel surfaces of different polarities following arc ablation. For steel(−)–carbon(+), the low-magnification morphology showed no significant difference from that observed in static tests; however, high-magnification views revealed distinct features: the steel surface was covered with numerous aggregates of micron-sized molten particles of similar dimensions, accompanied by a small number of fine, discontinuously distributed microcracks. A network of cracks formed on the surface of the remelted layer; these cracks were relatively wide and extended outwards into fine cracks, whilst a large number of circular micro-pores were dispersed throughout.

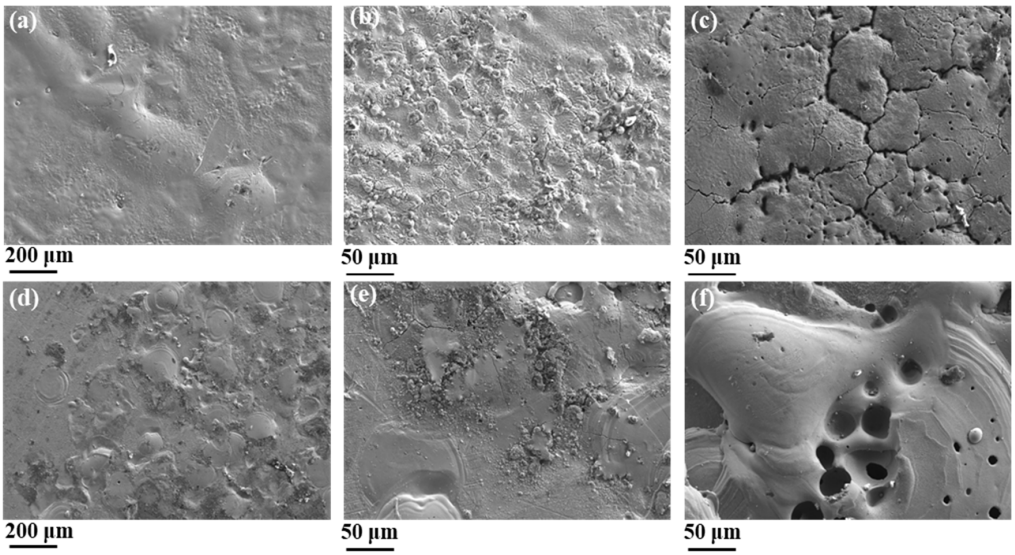


Figure 13. Microscopic morphology of steel surfaces after dynamic tests: (**a**–**c**) steel as cathode; (**d**–**f**) steel as anode.

For steel(+)–carbon(−), the low-magnification view was filled with circular or near-circular arc ablation pits, with a maximum diameter approaching 200 μm. The pit boundaries were distinct, with some exhibiting multi-layered nested features; the matrix regions between the pits were covered with molten deposits, debris and carbon deposits. Under high magnification, dense molten particles, fractured remelted layers and loose deposited structures were visible around the pits, along with through-cracks along the pit edges. Flow ripples and solidification folds formed by the rapid cooling of molten steel were present, interspersed with circular gas pores of varying sizes.

Figure 14 shows SEM images (×50, ×200, ×300) of the ablated regions on the surfaces of carbon brushes of different polarities following arc ablation. For steel(−)–carbon(+): Overall surface damage was minor; at low magnification, a large, white, hazy coating was visible on the carbon brush surface. EDS mapping of the bright coating shown in Figure 15b revealed local Fe enrichment, indicating that it was an Fe-containing deposit rather than confirming a specific metallic or oxide phase. At high magnification, spherical molten

particles were observed within the white coating, accompanied by the formation of cracks, whilst the graphite matrix exhibited signs of spalling; the damage was relatively shallow.

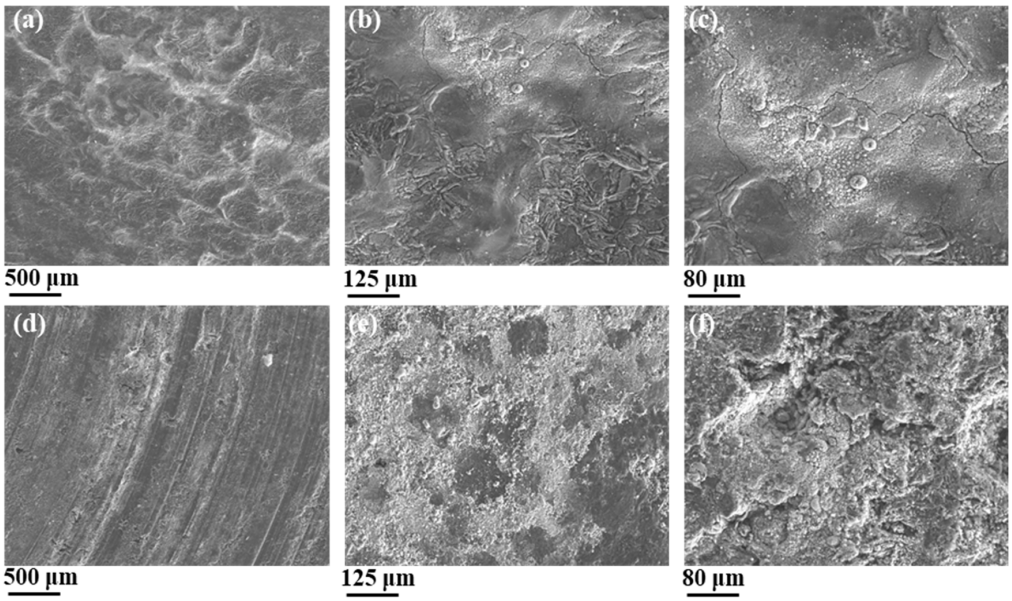


Figure 14. Microscopic morphology of carbon brush surfaces after dynamic tests: (**a**–**c**) carbon as anode; (**d**–**f**) carbon as cathode.

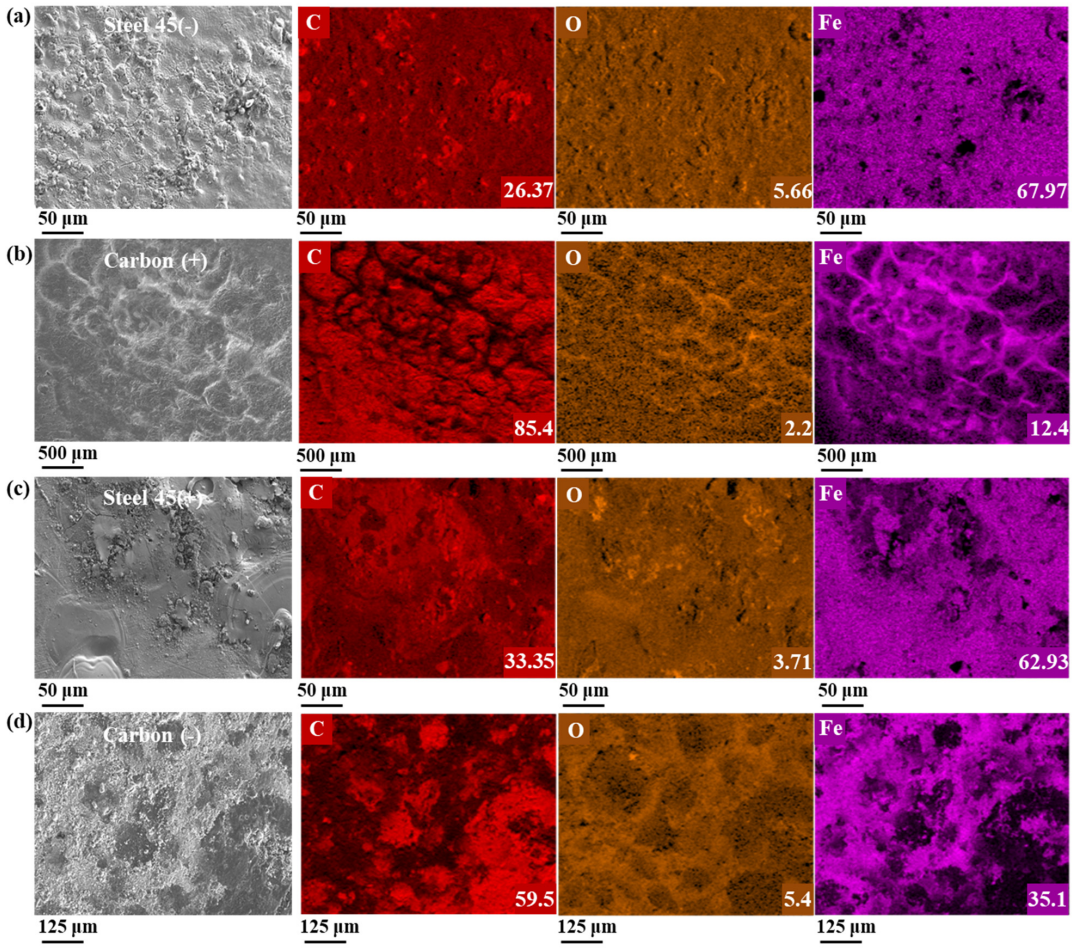


Figure 15. Elemental distribution and concentrations in ablated regions after dynamic tests: (**a**) steel as cathode; (**b**) carbon as anode; (**c**) steel as anode; (**d**) carbon as cathode.

For steel(+)–carbon(−): During rotation, the arc root swept across the graphite matrix, causing etching pits and delamination of the graphite layer at the etched sites. At high magnification, the graphite matrix was covered by extensive white molten deposits and metal particles; the matrix structure exhibited widespread interlaminar cracking, disintegration and delamination, losing the original layered continuity of the graphite.

Figure 15 shows the elemental distribution and concentrations in the ablated regions of the steel and carbon surfaces following dynamic arc ablation. For steel(−)–carbon(+): the three elements were uniformly distributed across the scanned area on the steel surface, with a slight accumulation of elements at the melted particles, corresponding to a slight reduction in Fe distribution at these locations. Quantitative analysis revealed C and O contents of 26.37 wt.% and 5.66 wt.%. Compared with those measured on the unablated steel reference surface, these values corresponded to increases of 19.87 and 4.16 percentage points, respectively. EDS analysis of the white, hazy coating on the carbon surface revealed the presence of Fe and O, providing evidence consistent with the deposition of Fe-containing species transferred from the steel-disc cathode. The selected-area normalized EDS fractions of C, O, and Fe in this region were 85.3 wt.%, 2.2 wt.%, and 12.4 wt.%, respectively.

For steel(+)–carbon(−): The carbon content on the steel surface reached as high as 33.35 wt.%, exhibiting distinct cluster-like and patchy enrichment; oxygen was simultaneously enriched in the carbon-enriched zones, whilst the iron content decreased to 62.93 wt.%. On the carbon surface, the selected-area C fraction decreased to 59.5 wt.% and exhibited a localised patchy distribution. Fe and O were enriched in regions with relatively weak C signals. The Fe fraction reached 35.1 wt.%, corresponding to an increase of 34.8 percentage points relative to the unablated carbon reference surface, while the O fraction reached 5.4 wt.%.

3.4. Polarity Effects in Arc Damage to Steel/Carbon Friction Pairs

3.4.1. Physical Basis of Arc Polarity Effects and Material Coupling Mechanisms

The microscopic process of arc formation is illustrated in Figure 16. During the initial stage of discharge, free electrons are emitted from the cathode surface through thermo-field emission. The emitted electrons are accelerated by the electric field across the gap and undergo inelastic collisions with neutral particles, initiating impact ionization. Once the density of charged particles reaches the electrical breakdown threshold, the electrical conductivity of the gap increases abruptly, a stable plasma channel is established, and a self-sustained arc discharge is initiated [22].

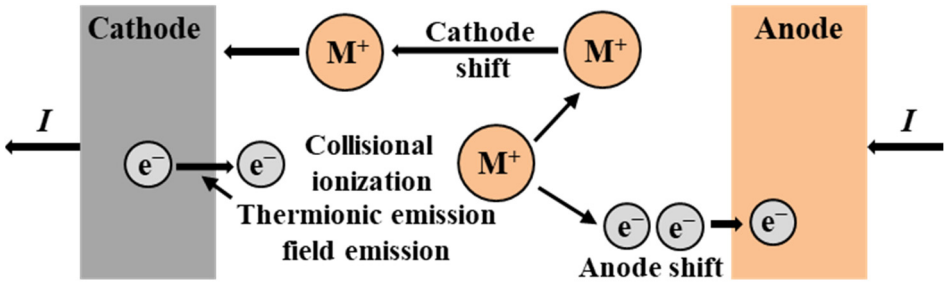


Figure 16. Schematic diagram of the microscopic physical processes involved in arc formation.

The essence of arc-induced damage lies in the asymmetric distribution of energy between the cathode and the anode after gas breakdown and the formation of a high-temperature plasma channel. During gap breakdown, free electrons are emitted from the cathode surface and accelerated into the plasma region by the electric field, whereas positive ions migrate towards the cathode and bombard the surface at high velocity [23,24]. Consequently, polarity not only changes the migration direction of

charged particles but also regulates cathode-spot behaviour, arc-root stability, and the distribution of thermo-mechanical loads at the interface, thereby leading to distinct damage characteristics.

From the perspective of energy partitioning in the near-electrode regions, the cathode and anode exhibit different energy-exchange mechanisms. At the cathode, energy input may include positive-ion bombardment and neutralization as well as Joule heating within the electrode, whereas electron emission and material evapouration may contribute to energy dissipation. Numerical modelling of atmospheric-pressure arc cathodes has further shown that the near-cathode sheath strongly affects charged-particle and energy transport, while Joule heating and the energy delivered by charged particles can make substantial contributions to cathode heating [25]. The emitted electrons can remove energy from the cathode surface by overcoming the material work function [26,27]. At the anode, incident electrons and energy transport through the near-anode plasma layer contribute to surface heating. Models of short atmospheric-pressure arcs and high-pressure anode regions indicate that the heat flux delivered to the anode is affected by the local current density, near-anode sheath, anode surface temperature, and current-transfer regime [28,29]. The relative contributions of these processes depend on the discharge conditions, electrode temperature, and attachment mode, resulting in different thermal responses of the cathode and anode [29,30].

Polarity-dependent damage is not determined solely by the total energy transferred to each electrode but is also strongly influenced by the spatial distribution of energy deposition. Localised cathodic attachment can produce high current density and heat flux within microscopic regions, resulting in concentrated thermal loading [25–27]. When carbon acts as the cathode, its porous and anisotropic microstructure may restrict local heat spreading and promote localised energy accumulation. Conversely, when steel serves as the cathode, its higher thermal conductivity facilitates heat redistribution and may reduce prolonged heating at a single location. Therefore, the asymmetry in cathode–anode energy exchange, combined with material-dependent heat-transfer characteristics, contributes to the different damage responses of the steel and carbon electrodes under opposite polarity configurations.

In steel/carbon systems, the polarity effect is strongly influenced by the intrinsic physical properties of the two materials. Steel can undergo localised melting, liquid flow, and subsequent resolidification, while its relatively high thermal conductivity facilitates the redistribution of localised heat input. In contrast, the carbon brush has a porous and anisotropic microstructure and does not readily form a stable molten layer under atmospheric-pressure conditions. Its surface degradation may instead involve sublimation, oxidation, pore expansion, and interlayer delamination [23,31]. These characteristics may promote localised energy accumulation and solid-state degradation around surface defects, thereby contributing to the observed polarity-dependent damage.

3.4.2. Interface Energy Distribution and Material Transport Mechanisms

When steel(+)–carbon(−) is employed, the steel-side interface is subjected to bombardment by high-energy electrons. Heat flux becomes highly concentrated at surface asperities, defects in the oxide film, and other microstructural discontinuities, resulting in the formation of a locally constricted anode arc root. The concentrated energy input can generate extremely high local temperatures, potentially causing rapid melting and vapourization of steel [32].

The recoil pressure generated by rapid vapour expansion, together with plasma flow and electromagnetic forces, induces severe molten-pool instability [33]. When these driving forces exceed the restraining effect of surface tension, molten metal is ejected

from the interface as high-velocity droplets, which become spheroidized during flight and rapidly solidify into deposited particles [34]. The arc root repeatedly extinguishes and reignites at the crater edge, resulting in the characteristic nested growth of erosion pits. Meanwhile, the ejection of a large number of molten droplets and metal vapour removes part of the input energy from the discharge region, thereby reducing sustained heat accumulation at the interface.

The observed elemental redistribution and surface deposits provide evidence consistent with bidirectional interfacial material transfer during arc discharge. Carbon vapour and fine carbonaceous species generated from the carbon cathode may be transported toward the steel surface and deposited within the molten region, leading to carbon enrichment. This is consistent with the carbon enrichment detected on the steel surface after arc ablation. Conversely, micrometer-sized molten iron droplets and evapourated iron species generated from the steel side migrate toward the carbon side and form iron-rich deposits, corresponding to the Fe-containing regions identified on the carbon surface. The carbon cathode is simultaneously subjected to positive-ion bombardment, localised heating at cathode spots, and impacts from molten metal droplets. In addition, the porous and anisotropic structure of graphite provides preferential attachment sites for cathode spots, facilitating repeated arc attachment at localised regions and thereby enhancing local energy accumulation. As a result, the carbon cathode exhibits a substantially higher measured net mass loss rate.

When steel(−)–carbon(+) is employed, the steel side is primarily subjected to positive-ion bombardment, while the discharge is sustained by thermo-field electron emission. Cathode spots on a uniform metallic surface exhibit self-diffusion characteristics and can migrate toward regions with lower work function, thereby preventing prolonged energy concentration within a single micro-region and promoting a more uniform distribution of heat input.

The steel surface primarily undergoes overall melting and liquid spreading. Under the action of surface tension, a continuous molten layer is formed and subsequently solidifies into a dense remelted layer after arc extinction. Only localised regions develop network-like thermal-stress cracks due to stress relaxation. This morphology is in excellent agreement with the smooth remelted layer and network-like crack patterns observed experimentally.

Because large-scale molten droplet ejection is absent, arc energy is retained within the system predominantly through interfacial heat conduction, resulting in significantly enhanced interfacial heat accumulation. The carbon anode undergoes only limited sublimation and oxidation, and the resulting carbon vapour and fine carbon particles migrate toward the steel side, where they contribute to interfacial deposition. In contrast, trace evapouration products from the steel cathode migrate toward the carbon side and form discrete deposits.

3.4.3. Mechanism of Arc-Root Evolution Under Dynamic Conditions

The dynamic test in the present study was conducted with a constant interelectrode gap and without mechanical contact. Rotation did not produce periodic contact separation or intentional variations in the geometric gap. Instead, it continuously changed the local steel surface positioned beneath the carbon brush and may also have modified the surrounding gas flow. These effects altered the arc-root attachment position and were associated with the observed intermittent extinction and reignition of the arc. Accordingly, the rotating test reflects the influence of circumferential relative motion on the spatial distribution of arc-induced damage under a controlled non-contact condition.

Under the steel(-)–carbon(+) configuration, cathode spots on the steel surface exhibit a strong tendency to migrate. The intrinsic migration of cathode spots prevents

prolonged arc attachment at a fixed location. Combined with the sweeping motion of the rotating disc, the arc root expands uniformly along the circumferential direction, preventing prolonged arc attachment at a specific location. Consequently, the dwell time at any individual location is further reduced, resulting in a more uniform spatial distribution of heat input and ultimately forming a continuous arc-shaped remelted zone distributed along the circumference.

Under the steel(+)–carbon(-) configuration, the anode arc root strongly depends on the electric-field enhancement induced by surface asperities. During rotation, these previously affected and newly exposed surface regions successively passed through the discharge region, causing periodic arc-root extinction followed by reignition at fresh asperities. Frequent re-ignition promotes preferential arc attachment to newly formed defect sites, thereby accelerating the growth and interconnection of erosion pits and ultimately producing a dense distribution of near-circular pits.

The centrifugal force generated by rotation further promotes molten-droplet detachment. Under the steel(+)–carbon(−) configuration, the ejected molten droplets are unlikely to refill their original locations, thereby increasing the net material loss. In contrast, under the steel(−)–carbon(+) configuration, the molten layer spreads tangentially under the combined effects of centrifugal force and surface tension before cooling uniformly, resulting in a smoother surface morphology.

From the perspective of practical operation of hydroelectric generator excitation systems, the polarity-dependent morphologies observed in this study correspond to different degradation pathways of the steel/carbon current-carrying friction pair. The steel(-)–carbon(+) configuration is mainly characterized by repeated thermal cycling, resulting in a continuous remelted layer and thermally induced cracks, which may gradually deteriorate contact stability during long-term operation. In contrast, the steel(+)–carbon(-) configuration exhibits an intensive material-removal mode with nested erosion craters, molten deposits, and severe surface roughening. Such damage promotes further arc attachment at surface defects and accelerates interface degradation. Therefore, polarity-dependent arc damage represents not only different surface morphologies but also distinct failure modes of the brush–slip ring system.

It should be noted that the conclusions of this study are based on low-current, non-contact arc-ablation conditions for a Steel 45/carbon friction pair, and the corresponding damage mechanisms are strongly coupled with the physicochemical properties of the two materials. Whether similar polarity-dependent mechanisms occur in other friction-pair materials or at different current levels requires further investigation.

4. Conclusions

Through static gap and dynamic tests, this study systematically investigated the polarity effect of arc damage in a Steel 45/carbon friction pair, and reached the following main conclusions:

1. Polarity-induced arc mode transition determines the macroscopic damage characteristics. Under the steel(+)–carbon(−) configuration, the arc exhibited unstable burst-like discharge accompanied by intense spark spattering, resulting in a wide severely ablated region dominated by material ejection. In contrast, the steel(−)–carbon(+) configuration produced a spatially constrained and stable arc, leading to a continuous thermally oxidized remelting zone. These results demonstrate that electrode polarity controls the evolution mode of arc-induced surface degradation.
2. The asymmetric degradation of carbon electrodes originates from polarity-dependent near-electrode energy transfer. When carbon acted as the cathode, positive-ion bombardment, localised cathode-spot heating, and molten metal droplet impact jointly ac-

celerated carbon degradation, resulting in a net mass loss rate approximately 2.5 times higher than that under anodic conditions. This reveals that the coupling between cathode energy concentration and graphite structural characteristics dominates carbon brush failure.

3. Electrode polarity determines distinct steel damage mechanisms through arc-root evolution. When steel served as the anode, constricted anode arc roots generated localised high energy density, causing micro-explosive ejection and nested erosion pits. When steel served as the cathode, cathode-spot migration promoted heat redistribution and produced a continuous remelted layer accompanied by thermal-stress cracks.
4. Bidirectional material migration: Selected-area EDS mapping revealed C enrichment on the steel surface and Fe enrichment on the carbon surface relative to the corresponding unablated reference surfaces. These complementary elemental-enrichment patterns provide evidence consistent with bidirectional transfer of carbon^{-} and Fe^{-} containing species between the two electrodes.
5. The polarity effect of arc ablation in the steel/carbon electrode pair was associated with the combined effects of near-electrode energy transfer, arc-root evolution, and bidirectional material migration. Under the fixed-gap non-contact rotating condition, rotational motion modified the spatial distribution of arc attachment and the resulting surface damage.

This study reveals the polarity-dependent characteristics and formation mechanisms of arc ablation in steel/carbon friction pairs, providing a theoretical basis for optimizing polarity configuration and developing differentiated protection strategies for hydroelectric generator slip rings.

Author Contributions: All authors contributed to the study conception and design. Material preparation was conducted by W.Y.; data collection and analysis were performed by W.L.; the initial draft was written by W.L., and manuscript review was completed by X.Z. (Xinze Zhao), X.X. and X.Z. (Xiaolong Zhang). All authors have read and agreed to the published version of the manuscript.

Funding: This study was supported by the National Natural Science Foundation of China (Grant No.52475202).

Data Availability Statement: All data that support the findings of this study are included within the article.

Conflicts of Interest: The authors declared no potential conflicts of interest with respect to the research, authorship, and/or publication of this article.

References

1. Zhao, M.Y.; Li, J.W.; Li, C.S.; Li, Y.Y.; Zhang, X.L. Study on Current-Carrying Friction Characteristics and Corrosion Resistance of Carbon Brush/Collector Ring by Copper–Graphene Electrodeposition Process. *Lubricants* **2025**, *13*, 162. [CrossRef]
2. Ai, Y.J.; Xie, J.H.; Lu, K. Analysis and Treatment of the Problem of Flashover of the Collector Ring of a Hydroelectric Generator in a Hydropower Plant. *J. Yunnan Electr. Power* **2024**, *52*, 27–32.
3. Shan, W.J. Analysis and Treatment of Excessive Temperature and Sparking of Carbon Brushes in Large Hydroturbine Generators. *J. Hydropower New Energy* **2021**, *35*, 47–49. [CrossRef]
4. Yang, Z.Y. Cause Analysis and Countermeasures for Carbon Brush Ring Fire Failure in Power Plant Generators. *J. Plant Maint. Eng.* **2021**, *8*, 47–49. [CrossRef]
5. Qin, H.L.; Wang, J.T.; Li, H.B.; Zhao, X.Z.; Yi, J.W.; Zhao, Y.J.; Ren, Z.Y. Effect of Operating Conditions on Friction Surface Film Formation of Carbon Brush/Slip Ring Assemblies. *J. Surf. Technol.* **2023**, *52*, 178–188. [CrossRef]
6. Gao, G.Q.; Fu, R.; Wang, Q.S.; Chen, J.H.; Qian, P.Y.; Zeng, J.J.; Weng, X.; Li, H.Y.; Yang, Z.F.; Wang, H.; et al. Progress on current-carrying friction and wear and prediction models: A review. *Friction* **2026**, *14*, 9441151. [CrossRef]
7. Nie, Y.J.; Guan, C.L. Research Progress on the Influence of Environmental Factors on the Current-Carrying Friction and Wear Performance of the Pantograph-Electrified Rail System. *Mech. Electr. Eng. Technol.* **2026**, 1–11. Available online: https://link.cnki.net/urlid/44.1522.TH.20260723.1536.003 (accessed on 1 August 2026). [CrossRef]

8. Shen, M.X.; Chen, S.Y.; Wu, H.H.; Xiao, L.; Wang, N.H.; Ji, D.H. Research Progress on the Current-Carrying Tribological Behaviour of Materials Under Service Environment Effects. *China Mech. Eng.* **2026**, *37*, 2–13.
9. Hui, Y.; Liu, G.M.; Yan, T.; Du, L.F.; Zhou, L. Research Status and Prospect of Current-carrying Friction and Wear. *Mater. Rep.* **2019**, *33*, 2272–2280.
10. Li, C.H.; Zhang, Y.Y.; Zeng, Z.X.; Niu, K.; Song, C.F.; Shangguan, B.; Zhang, Y.Z. Research Progress of Current-Carrying Friction and Wear. *Lubr. Eng.* **2022**, *47*, 153–167.
11. Zhao, H.; Feng, Y.; Zhou, Z.J.; Qian, G.; Zhang, J.C.; Huang, X.C.; Zhang, X.B. Effect of Electrical Current Density, Apparent Contact Pressure, and Sliding Velocity on the Electrical Sliding Wear Behaviour of Cu–Ti_3AlC_2 Composites. *Wear* **2020**, *444–445*, 203156. [CrossRef]
12. Wu, H.; Liu, C.; Niu, G.; Zhang, L.; Liu, H.; Kang, X. Effect of the Contact Load and Rotation Speed on the Formation of Rolling Current-Carrying Arc and the Corresponding Material Damage. *J. Mater. Res. Technol.* **2024**, *32*, 1696–1703. [CrossRef]
13. Wang, P.; Wu, K.; Wu, W.; Pan, A.; Guo, Z.; Chen, S. Current-Carrying Wear Behaviour of CoCrFeNiW0.2 and CoCrFeNiW0.2+3 at. % C High-Entropy Alloys. *Tribol. Int.* **2024**, *197*, 109749. [CrossRef]
14. Deng, C.Y.; Yin, J.; Zhang, H.B.; Xiong, X.; Wang, P.; Sun, M.; Wu, X.G. Dynamic Variation of Arc Discharge and Its Effect on Corrosion Direction under Current-Carrying Sliding. *Proc. Inst. Mech. Eng. Part J J. Eng. Tribol.* **2019**, *233*, 380–392. [CrossRef]
15. Yang, Z.H.; Zhang, Y.Z.; Zhao, F.; Shangguan, B. Dynamic Variation of Arc Discharge during Current-Carrying Sliding and Its Effect on Directional Erosion. *Tribol. Int.* **2016**, *94*, 71–76. [CrossRef]
16. Zhang, Y.; Zhang, Y.; Song, C. Arc Discharges of a Pure Carbon Strip Affected by Dynamic Contact Force during Current-Carrying Sliding. *Materials* **2018**, *11*, 796. [CrossRef] [PubMed]
17. Tang, W.; Zhao, X.K.; Qin, H.L.; Ji, Y.B.; Zhu, F.D.; Li, Y.F.; Su, Q.D.; Yang, Z.Y.; He, W.; Zhao, X.Z. The Influence Mechanism of Slip Ring Material Characteristics on Arc Erosion Resistance. *Wear* **2026**, *601*, 206833. [CrossRef]
18. Jin, W.B.; Chen, S.K.; Yang, Z.F. Effect of Polarity on Electrode Material Arc Ablation. *J. Electr. Energy Manag. Technol.* **2019**, *3*, 1–5. [CrossRef]
19. Liu, Z.W.; Chen, S.K.; Li, C.K.; Zhu, Y.L.; Gao, J.F. Analysis of Arcing Characteristics of Carbon–Copper Electrodes under Different Polarities. *J. Electr. Energy Manag. Technol.* **2020**, *2*, 25–29. [CrossRef]
20. Zhao, X.Z.; Chen, M.; Nie, Y.F.; Li, X.Q.; Xiao, S.L.; Xu, X. Experimental Study on Gap Discharge between the Carbon Brush and Slip Ring Interface of a Hydroelectric generator. *J. Water Resour. Power* **2022**, *40*, 169–172. [CrossRef]
21. Xiao, S.L.; Li, C.S.; Zhao, X.Z.; Li, X.Q.; Chen, M. Influence of Wear Products on Discharge at the Current-Carrying Friction Interface. *J. Lubr. Eng.* **2024**, *49*, 116–124.
22. Qin, H.L.; Xiao, J.W.; Tang, W.; Gu, W.K.; Li, M.; Sang, X.T.; Wu, S.Q.; He, W.; Zhao, X.Z. Polarity Effect of Current-Carrying Friction Pairs and Its Influence on Surface Damage. *J. China Surf. Eng.* **2025**, *38*, 171–183.
23. Wu, G.N.; Zhou, Y.; Gao, G.Q.; Wu, J.; Wei, W.F. Arc erosion characteristics of Cu-impregnated carbon materials used for current collection in high-speed railways. *IEEE Trans. Compon. Packag. Manuf. Technol.* **2018**, *8*, 1014–1023. [CrossRef]
24. Liao, Q.H.; Wei, W.F.; Zuo, H.Z.; Li, X.B.; Yang, Z.F.; Xiao, S.; Wu, G.N. Interfacial bonding enhancement and properties improvement of carbon/copper composites based on nickel doping. *Compos. Interfaces* **2021**, *28*, 651–663. [CrossRef]
25. Sun, L.; Sun, X.P.; Guo, B.Y.; Zhou, W.; Li, Z.Y. Unified modeling and kinetic analysis of the near-cathode region and hot cathode in atmospheric-pressure arc discharges. *J. Phys. Fluids* **2022**, *34*, 067120. [CrossRef]
26. Anders, A. Glows, arcs, ohmic discharges. An electrode-centered review on discharge modes and the transitions between them. *Appl. Phys. Rev.* **2024**, *11*, 031310. [CrossRef]
27. Benilov, M.S. Understanding and modelling plasma–electrode interaction in high-pressure arc discharges: A review. *J. Phys. D Appl. Phys.* **2008**, *41*, 144001. [CrossRef]
28. Santos, D.F.N.; Almeida, N.A.; Lisnyak, M.; Gonnet, J.-P.; Benilov, M.S. Numerical investigation of regimes of current transfer to anodes of high-pressure arc discharges. *Phys. Plasmas* **2022**, *29*, 043503. [CrossRef]
29. Khrabry, A.; Kaganovich, I.D.; Nemchinsky, V.; Khodak, A. Investigation of the short argon arc with hot anode. II. Analytical model. *Phys. Plasmas* **2017**, *25*, 013522. [CrossRef]
30. Heberlein, J.; Mentel, J.; Pfender, E. The anode region of electric arcs: A survey. *J. Phys. D Appl. Phys.* **2010**, *43*, 023001. [CrossRef]
31. Xie, W.H.; Wu, G.N.; Yang, Z.F.; She, P.P.; Wang, H.; Zuo, H.Z.; Wei, W.F.; Gao, G.Q.; Tu, C.J. Study on the erosion characteristics of copper–carbon electrode pairs by DC air arc. *High Volt.* **2021**, *6*, 674–683. [CrossRef]
32. Nemchinsky, V.A.; Showalter, M.S. Cathode erosion in high-current high-pressure arc. *J. Phys. D Appl. Phys.* **2003**, *36*, 704–712. [CrossRef]
33. Rong, M.Z.; Wu, Y.; Niu, C.P. *Electrical Contact Theory and Applications*; China Machine Press: Beijing, China, 2013; pp. 73–127.
34. Gray, E.W.; Pharney, J.R. Electrode erosion by particle ejection in low-current arcs. *J. Appl. Phys.* **1974**, *45*, 667–671. [CrossRef]

Disclaimer/Publisher's Note: The statements, opinions and data contained in all publications are solely those of the individual author(s) and contributor(s) and not of MDPI and/or the editor(s). MDPI and/or the editor(s) disclaim responsibility for any injury to people or property resulting from any ideas, methods, instructions or products referred to in the content.